Mechanics of Advanced Materials and Structures

ISSN: (Print) (Online) Journal homepage: www.tandfonline.com/journals/umcm20

Experimental and computational study of the NiTi thin wires mechanical behavior

Ekaterina S. Marchenko, Alexander A. Kozulin, Anna V. Vetrova, Marina A. Kovaleva, Alex A. Volinsky & Kirill M. Dubovikov

To cite this article: Ekaterina S. Marchenko, Alexander A. Kozulin, Anna V. Vetrova, Marina A. Kovaleva, Alex A. Volinsky & Kirill M. Dubovikov (18 Apr 2024): Experimental and computational study of the NiTi thin wires mechanical behavior, Mechanics of Advanced Materials and Structures, DOI: 10.1080/15376494.2024.2342031

To link to this article: https://doi.org/10.1080/15376494.2024.2342031

MECHANICS OF ADVANCED MATERIALS AND STRUCTURES
https://doi.org/10.1080/15376494.2024.2342031

Taylor & Francis
Taylor & Francis Group

ORIGINAL ARTICLE

Experimental and computational study of the NiTi thin wires mechanical behavior

Ekaterina S. Marchenko[a,b], Alexander A. Kozulin[a], Anna V. Vetrova[a], Marina A. Kovaleva[a], Alex A. Volinsky[a,c], and Kirill M. Dubovikov[a]

[a]Laboratory of Medical Alloys and Shape Memory Implants, National Research Tomsk State University, Tomsk, Russia; [b]Institute for Problems of Chemical and Energy Technologies, Siberian Branch of the Russian Academy of Sciences, Biysk, Russia; [c]Department of Mechanical Engineering, University of South Florida, Tampa, Florida, USA

ABSTRACT

NiTi wires used for biological implants demonstrated ductile fracture. NiTi 40, 60, and 90 μm thick wires were tested in uniaxial tension to fracture and loading-unloading. Uniaxial stress-strain curves demonstrate superelastic behavior. The inelastic martensite transformation strain is completely recovered upon unloading, forming thermo-mechanical hysteresis. A mathematical model was developed to describe superelasticity effects in NiTi wires. Modeling results are qualitatively and quantitatively similar to experimental data, and capture elastic deformation of austenite, forward martensite phase transformation stress plateau before the onset of martensite elastic deformation and the entire unloading range. The elastic limit and strength increase with the wire thickness.

ARTICLE HISTORY
Received 22 January 2024
Accepted 8 April 2024

KEYWORDS
NiTi wire; tensile loading; stress hysteresis; modeling; superelasticity

1. Introduction

Nitinol (NiTi) is an intermetallic compound of nickel and titanium in almost equiatomic quantities (50–51 at.% Ni). NiTi belongs to the class of shape memory alloys (SMA), which have unique properties of superelasticity and shape memory [1]. The shape memory effect was first used in industry. The first successful engineering applications in the 60s and 70s used limited recovery of SMA for joining and fastening [2]. Superelastic NiTi can recover 6–8% strain through the reversible stress-induced martensitic transformation, where the B2 austenitic phase transforms into B19' monoclinic martensite under the so-called upper stress plateau. In recent decades, the superelasticity effect has been used in several applications, including the development of alternative thermal cooling methods [3, 4]. Elastocaloric cooling is particularly attractive due to its efficiency in creating large temperature ranges (differences between hot and cold regions) [5–7].

The superelastic properties of NiTi are widely used for medical purposes [8]. NiTi is particularly attractive for the manufacture of implants, such as stents, vena cava filters, metal hosiery, and transcatheter heart valves for minimally invasive medical interventions. Unlike other bioinert metals that are used to make stents and require plastic deformation to expand the capillary wall, NiTi stents are self-expanding. That is, they are compressed from an open configuration, loaded into the catheter, and then deployed. When deployed, the stent self-expands and exerts the necessary radial force to keep the capillary open. Typically, the stent outer diameter is ~10% larger than the capillary to restore blood flow and ensure reliable stent fixation [8]. Thus, the device is never completely unloaded after deployment, leaving it in a state of mixed austenite and martensite phase. Once deployed, NiTi stents experience loading from cardiac cycles, respiration, and musculoskeletal movements [9]. The deployment and loading of a device determine its operating average strain and "loading-unloading" strain, respectively. Metal knitwear made of superelastic NiTi wire is also highly promising for reconstructive surgery of bone and soft tissues [10–14].

Currently, there are many physical and mathematical models for numerical calculations of the stress-strain state of a structure made of SMA. For example, there is a thermomechanical model that can realistically simulate several physical phenomena, including the interphase transition, as well as the reorientation of martensite, which can simultaneously occur under a common thermomechanical load [15–17]. The paper [18] evaluated fatigue life based on strain amplitude, temperature, and cycle frequency. There is also a model based on equivalent strain to estimate the number of cycles before failure of NiTi alloys used in medical devices under multiaxial loads [19]. The paper [20] examines the study of the finite deformation bending of shape-memory wires that takes cognizance of the dissipative nature of the body under consideration. The contribution [21] presents the kinetostatic analysis of a spatial compliant mechanism actuated by three SMA wire actuators.

There are many examples in the literature of physical and mathematical models of SMA that have been developed specifically to describe the thermomechanical behavior of NiTi in a

CONTACT Kirill M. Dubovikov kirill_dubovikov@mail.ru Laboratory of Medical Alloys and Shape Memory Implants, National Research Tomsk State University, 36 Lenin Ave., Tomsk, 634045, Russia.

manner (including superelastic-plastic effects, inelastic stress accumulation due to fatigue, shape memory). However, they require a significant number of input parameters and, therefore, multiple experiments to evaluate them. There is work in which a simple one-dimensional model was used to analyze limited recovery in an SMA wire. The model is based on the generalized plasticity theory developed by Lubliner and Auricchio [22, 23]. The finite element simulation software Ansys Mechanical allows the use of the Auricchio constitutive model [24] for superelastic materials. It can capture the most important aspects of a superelastic material using just seven parameters that can be obtained from experimental results. Moreover, this model allows one to take into account the tension-compression asymmetry, which affects the localization of stresses and strains in NiTi during bending. The rheological description and the mechanical behavior of microwires should be taken into account when developing physical and mathematical models and carrying out numerical calculations of the stress-strain state of both the wire itself and products made from it under constant and alternating loads. As mentioned earlier, many papers are dedicated to modeling NiTi wires' behavior during bending, tension, or damping, however, most literature reports consider thicker wires over 1 mm in diameter [25, 26]. These wires with larger diameter are not applicable for medical purposes because thinner wires with <1 mm thickness must be used for stents [27, 28]. Some experimental investigations demonstrate mechanical properties dependence on the wire diameter, including copper wires [29]. In earlier work we reported experimental results that demonstrated the existence of mechanical properties dependence on the NiTi wire diameter [30]. At the same time, we didn't find theoretical papers confirming these effects in NiTi. Therefore, the aim of this work is to investigate the dependence of the NiTi mechanical properties on the wire diameter using the Auricchio model based on experimental results of stretching wires with 40, 60, and 90 μm thickness. The results obtained in this work will expand the existing knowledge about the deformation behavior of micrometer-thick wires and also allow to create metallic knitwear in accordance with individual patient requirements [31].

The purpose of this research is to assess the mechanical behavior of NiTi microwires to create physical and mathematical models for assessing the stress-strain state using numerical methods.

2. Materials and methods

NiTi wires (Ti-50 at.% Ni) with 40, 60, and 90 μm thickness were obtained from 240 × 20 mm monolithic ingots using thermomechanical processing with intermediate annealing in four stages, sequential multi-cycle strip rolling, rotational forging of rods, cold and hot drawing:

1. Straight rolling of an ingot with a 20 mm diameter to a 7 mm thick rod in 20 cycles at 1050 °C for 2 min;
2. Rotary forging of rods from 7 to 3.5 mm thickness in 7 cycles at 950 °C for up to 1 min;
3. Cold wire drawing from 3.5 mm to 500 μm in 25 cycles at 750 °C for 30 s;
4. Hot wire drawing from 500 to 90–40 μm in 50–70 cycles at 450 °C for 20 s.

NiTi wire with a 90 μm diameter is shown in Figure 1. Stress-strain curves for NiTi wires were obtained using a custom-built tensile testing machine at 0.1 mm/s deformation speed. Tensile elongation was monitored using a built-in displacement sensor with a 3 μm resolution, while simultaneously recording the developed force in the samples with a 0.004 N resolution accuracy. Fracture surfaces of the wires for scanning electron microscopy (SEM) and energy dispersive spectroscopy (EDS) characterization were obtained using a portable universal tensile testing machine Micron Test (Tomsk, Russia) [32] at room temperature and 0.1 mm/s deformation speed. The length of the tested wires was 150 mm. Images of the fracture surfaces of NiTi wire were obtained using a TESCAN MIRA3 LMU scanning electron microscope (SEM, 20 kV).

The uniaxial tension of superelastic NiTi wires was described by a standard system of continuum mechanics equations and solved by the finite element method in the Lagrangian formulation using the Ansys Workbench software package. The constitutive equation given by Auricchio [33] was used based on the experimental data, taking into account the NiTi wire superelastic behavior under loading and unloading to obtain stress-strain curves using numerical methods.

The model takes into account two phase transformations from austenite to martensite and vice versa in the continuum approximation. The martensite ξ_M and the austenite ξ_A fractions add to 1:

$$\xi_M + \xi_A = 1 \tag{1}$$

The material mechanical behavior is isotropic. The pressure dependence of phase transformation is modeled using the Drucker-Prager load function:

$$F = q + 3\alpha p \tag{2}$$

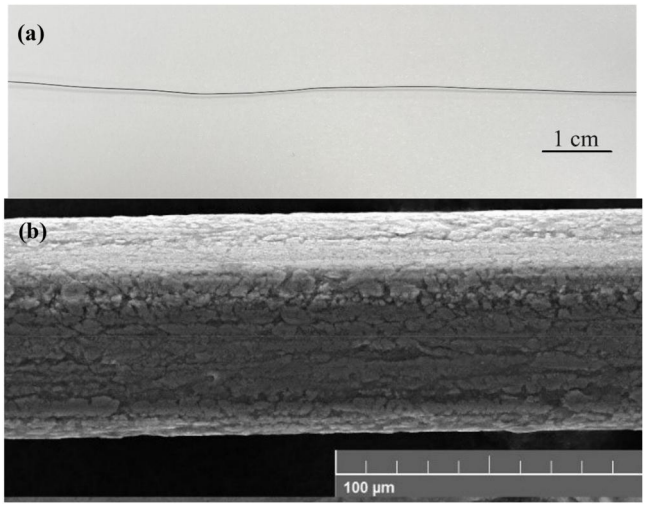

Figure 1. (a) Macroscopic view of 90 μm NiTi wire, (b) scanning electron microscopy image of 90 μm NiTi wire side.

$$q = \sqrt{\frac{3}{2} S{:}S} \tag{3}$$

$$S = \sigma - p\mathbf{1} \tag{4}$$

$$p = \frac{1}{3}\sigma{:}\mathbf{1} \tag{5}$$

Here, α is the material parameter, σ is the stress, $\mathbf{1}$ is the unit tensor, and S is the deviatoric part of the stress tensor. In this case, the martensite fraction ξ_M is determined as:

$$\dot{\xi}_S = \begin{cases} -H^{AM}(1-\xi_M)\dfrac{\dot{F}}{F - R_f^{AM}} & A \rightarrow M \text{ transition} \\ H^{MA}\xi_M \dfrac{\dot{F}}{F - R_f^{MA}} & M \rightarrow A \text{ transition} \end{cases} \tag{6}$$

where

$$R_f^{AM} = \sigma_f^{AM}(1 + \alpha) \tag{7}$$

$$R_f^{MA} = \sigma_f^{MA}(1 + \alpha) \tag{8}$$

$$H^{AM} = \begin{cases} 1, & \text{if} \begin{cases} R_M^{AM} < \mathrm{F} < R_f^{AM} \\ \dot{F} > 0 \end{cases} \\ 0 & \text{otherwise} \end{cases} \tag{9}$$

$$H^{MA} = \begin{cases} 1, & \text{if} \begin{cases} R_f^{MA} < \mathrm{F} < R_M^{MA} \\ \dot{F} < 0 \end{cases} \\ 0 & \text{otherwise} \end{cases} \tag{10}$$

$$R_M^{AM} = \sigma_M^{AM}(1 + \alpha) \tag{11}$$

$$R_M^{MA} = \sigma_M^{MA}(1 + \alpha) \tag{12}$$

Here, σ_f^{AM}, σ_f^{MA}, σ_M^{AM}, and σ_M^{MA} are material parameters listed in Table 1. The material parameter α characterizes the material response under tension and compression but was not taken into account in this work, since the load was only tensile, so $\alpha = 0$. The stress-strain relationship is expressed as:

$$\sigma = D{:}(\varepsilon - \varepsilon_{tr}) \tag{13}$$

$$\dot{\varepsilon}_{tr} = \dot{\xi}\,\bar{\varepsilon}_L \frac{\partial \mathrm{F}}{\partial \sigma} \tag{14}$$

Here, $\boldsymbol{D}$ is the elastic moduli matrix and ε_{tr} is the transition strain tensor.

The problem of the wire uniaxial tension was solved in a three-dimensional spatial formulation. Representative volumes in the form of 40, 60, and 90 µm diameter cylindrical 400, 600, and 900 µm long samples were used as geometric models of wires in Figure 2. Boundary conditions were specified as one fixed end and displacements of the other end along the cylinder axis:

$$u_x(0,y,z) = 0,\ u_y(0,y,z) = 0,\ u_z(0,y,z) = 0,\ u_x(L,y,z) = u_0 \tag{15}$$

where u_i are the components of the displacement vector, and u_0 is the magnitude of the tensile displacements.

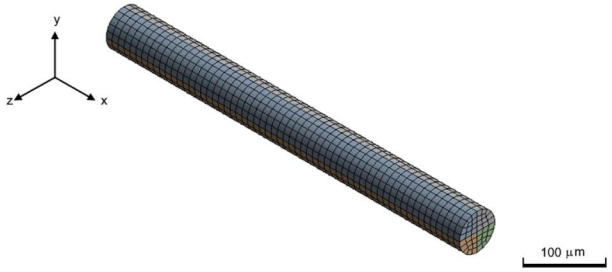

Figure 2. Finite element model of the wire under study.

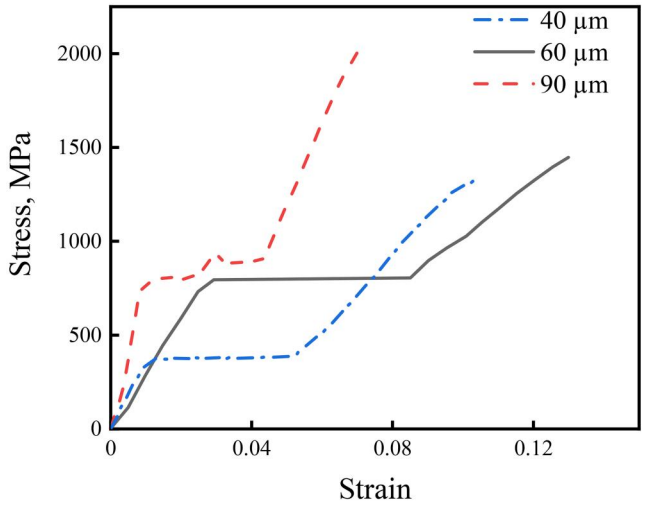

Figure 3. Uniaxial tension stress-strain curves of 40, 60, and 90 µm NiTi wires tested to failure.

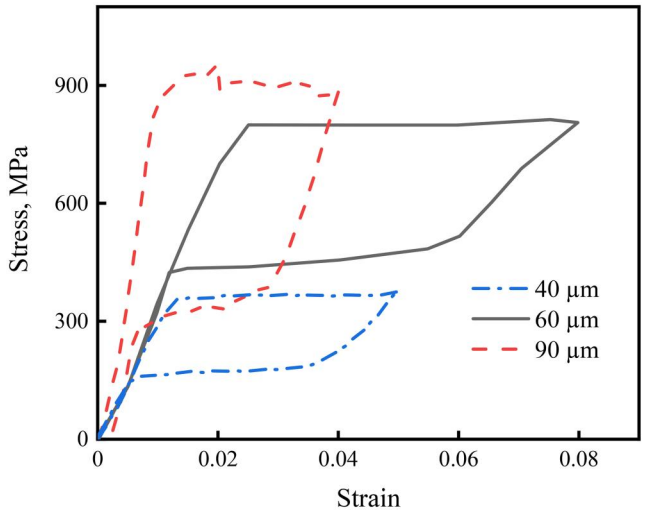

Figure 4. Uniaxial tension engineering stress-strain curves for 40, 60, and 90 µm NiTi wire under a single loading-unloading cycle.

Table 1. Superelasticity parameters for the governing constitutive equation.

Wire diameter (µm)	E_A (GPa)	σ_M^{AM} (MPa)	σ_f^{AM} (MPa)	σ_M^{MA} (MPa)	σ_f^{MA} (MPa)	$\bar{\varepsilon}_L$	α	E_M (GPa)
40	30	359	379	191	157	0.03	0	19
60	31	797	808	505	425	0.03		15
90	90	846	900	394	266	0.02		45

3. Results and discussions

3.1. Mechanical tests

NiTi 40, 60, and 90 µm thick wire samples were tested using uniaxial tension to fracture (Figure 3) and uniaxial loading-unloading tension cycles (Figure 4) in accordance with ASTM F2516-22.

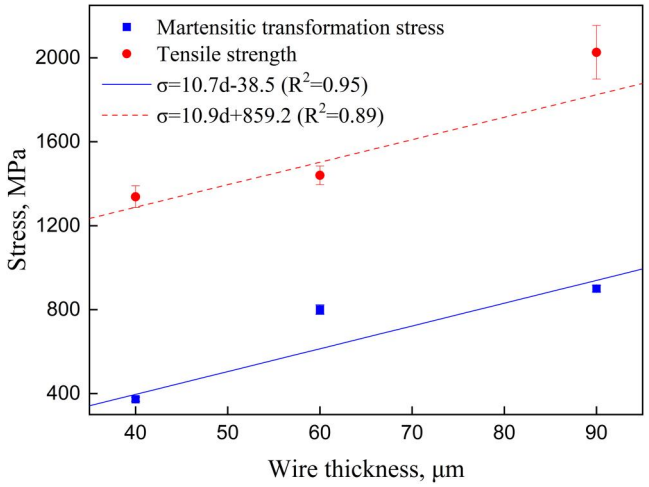

Figure 5. Martensitic transformation stress and tensile strength dependence on wire thickness.

All uniaxial tension stress-strain curves to fracture have three characteristics in Figure 3. There's austenite elastic deformation of up to 1% for 40 and 90 µm wires, and up to 3% for 60 µm wire. There's martensitic transformation at 1–5.5, 3–9, and 1–4.5% for 40, 60, and 90 µm wires, respectively. Finally, there's linear martensite deformation at 5.5–11% for 40 µm, 3–9% for 60 µm, and 4.5–7% for 90 µm thick wire. Martensitic shear stresses develop when the elastic limit is reached. Martensite propagates in the sample under constant stress, and a stress plateau is associated with the growth of martensite bands. The plateau stress coincides with the elastic limit, which is the maximum 846 MPa for a 90 µm wire, and the minimum 359 MPa for a 40 µm wire.

The deformation behavior of all samples is superelastic during the loading-unloading cycle. In tension, inelastic martensitic strain is completely restored upon unloading, resulting in mechanical hysteresis $\Delta\sigma$. The stress hysteresis is 200, 400, and 600 MPa for 40, 60, and 90 µm wires, respectively. The area of the superelastic hysteresis curve corresponds to the dissipated mechanical energy due to internal friction during the movement of the austenite-martensite interfaces and

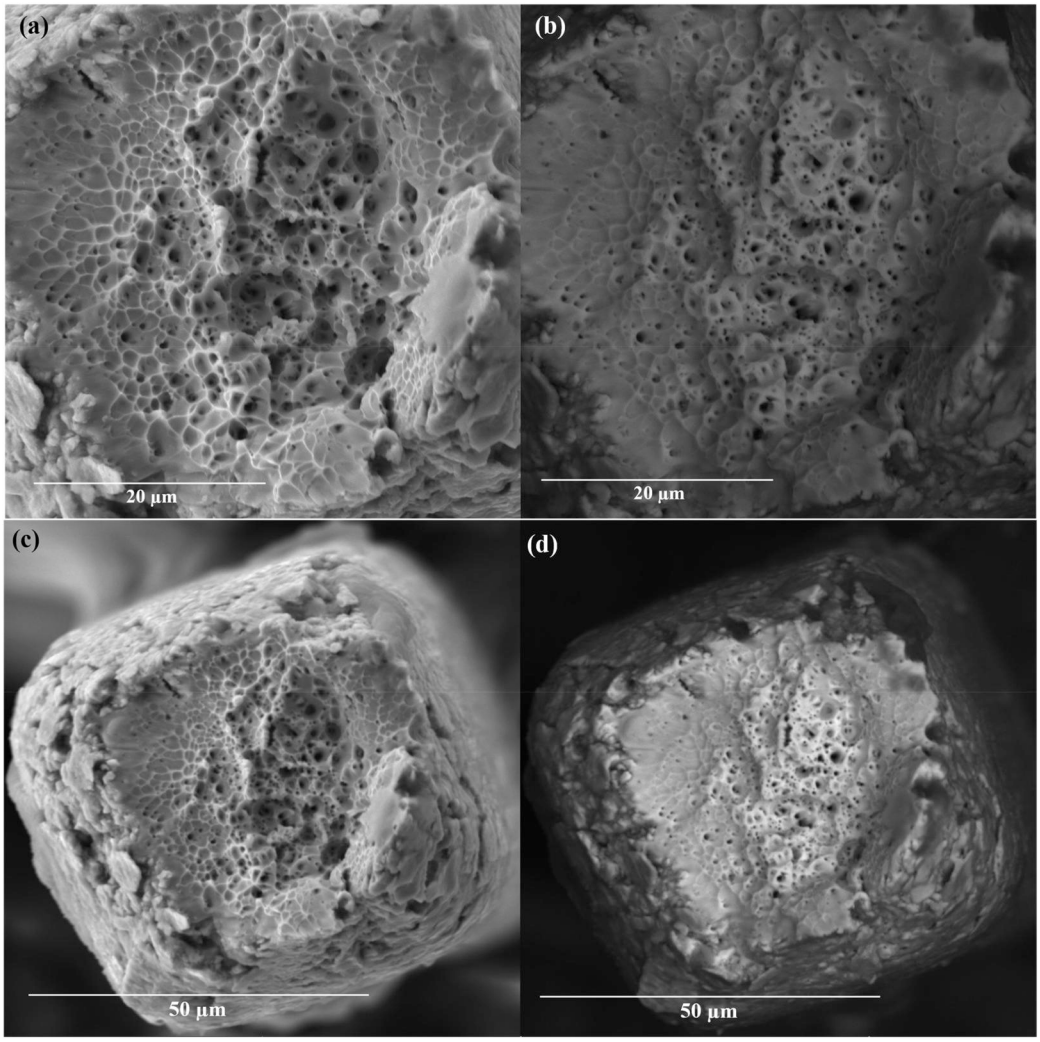

Figure 6. SEM images of NiTi 60 µm wire fracture surfaces: (a) secondary electrons (SE)—higher magnification, (b) backscatter secondary electrons (BSE)—corresponding phase contrast backscatter electron image, (c) SE—lower magnification image showing the whole fracture surface, (d) BSE—corresponding phase contrast backscatter electron image.

increases with wire thickness. The obtained engineering stress-strain curves correspond to typical NiTi behavior [30, 34, 35].

Figure 5 shows the mechanical properties dependence on the wire thickness. Both martensitic transformation stress (15) and tensile strength (16) increase with wire thickness in Figure 5. These properties can be approximated using linear equations:

$$\sigma_m = 10.7d + 38.5 \tag{16}$$

$$\sigma_B = 10.9d + 859.2 \tag{17}$$

Here, σ_m and σ_B is the martensitic transformation stress and tensile strength, respectively, and d is the wire thickness.

It is noted that the mechanical properties depend on the wire thickness. In this case, the strength of wires of different diameters at room temperature is 1314 ± 52, 1447 ± 45, and 2013 ± 128 MPa for 40, 60, and 90 μm thick wires. These strength values exceed the known monolithic polycrystalline TN-10, TN-20, and TN-1B NiTi-based alloys' strength of 740 ± 10, 820 ± 22, and 1110 ± 16 MPa [36]. This effect is explained by the nanocrystalline state of the wire material, formed by repeated thermal deformation during manufacturing, and precipitation, which easily can improve the strength of the NiTi by hundreds of MPa.

3.2. Microstructure studies

SEM images in Figure 6 show wire thinning at failure from 60 to 45 μm. Thinning and necking with limited ductility occurred due to the plastic shear of the viscous TiNi matrix. The fracture zone of the outer wire shell looks like a roller in Figure 6(c). The fracture surface appears as a pitted relief, having a typical appearance with particles at the bottom of the dimples in Figure 6(a). The final fracture zone is located in a depression in the center of the fracture zone, surrounded by zones of flattened relief in Figure 6(b). In this case, both parts have a viscous type of fracture. It is known that a flattened relief is formed by plastic shear during the slow crack growth, and a dimple relief is formed as a result of rapid viscous separation in the final fracture zone.

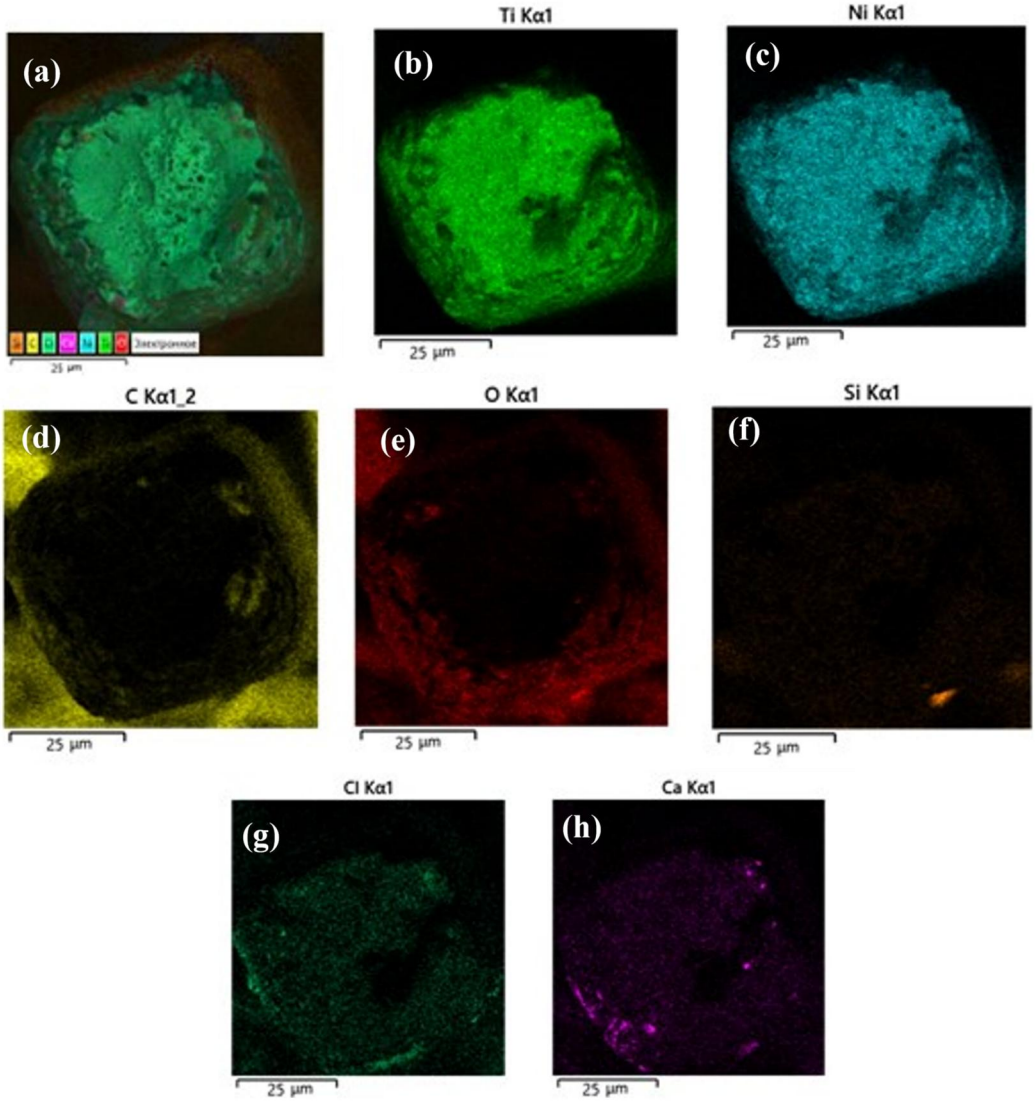

Figure 7. Elemental mapping of the 60 μm wire fracture surface: (a) combined elements map, (b) Ti, (c) Ni, (d) C, (e) O, (f) Si, (g) Cl, and (h) Ca maps.

The outer surface of the wire has a scaly relief formed due to the strong oxidation of the NiTi surface, forming layers of TiO_2.

Elemental analysis in Figures 7(a–h) shows a uniform distribution of titanium, nickel, and chlorine in the matrix, and an increased oxygen content in the surface layers, indicating that an oxide surface layer formed on the wire. In addition to oxygen, carbon, calcium, silicon, and chlorine-based inclusions were found in the wire outer shell. These maps were made to analyze fracture surfaces in more detail and identify possible inclusions that could serve as sources of cracks.

It can be argued that based on the discovered features of the relief and distribution of elements, the outer shell, enriched in nonmetallic phases, fractured by the brittle mechanism, and the center, consisting of the viscous TiNi phase, fractured by the ductile separation mechanism.

Surface phases are formed on the wire during the interaction of interstitial impurities with the surface layers of the TiNi matrix during cyclic plastic deformation and annealing in air in the presence of a lubricant in Figure 8. Interstitial impurities stimulate the matrix decomposition in the surface layers and the segregation of titanium to the surface.

NiTi characterization was performed using the equipment at Tomsk Regional Core Shared Research Facilities Center of the National Research Tomsk State University, supported by the grant from the Ministry of Science and Higher Education of the Russian Federation 075-15-2021-693 (No. 13.RFC.21.0012).

3.3. Modeling NiTi wire deformation

The formation of a complex stress state with inhomogeneous strain and stress fields in structures with complex geometry is confirmed by the numerical modeling analysis of experimental results. For further studies of the nature of the inhomogeneous stress-strain state of metal knitwear made of NiTi using solid-state geometric modeling methods, it is necessary to select and test a finite element model that describes the superelasticity of the NiTi alloy based on experimental results obtained by uniaxial tension of NiTi wires. The constitutive equation in the selected model includes 7 material constants obtained experimentally from uniaxial tensile stress-strain curves, listed in Table 1.

In Table 1, E_a and E_M are elastic moduli of the austenitic and martensitic phases, σ_M^{AM} and σ_f^{AM} are values of initial and final stresses for forward phase transition, σ_M^{MA} and σ_f^{MA} are values of the initial and final stresses for the reverse phase transition, ε_L is the maximum inelastic strain of the phase transition. The experimental methodology for determining material constants is presented in Figure 9.

Figures 10 and 11 show the calculated and experimental stress-strain curves of cyclic loading and uniaxial tension to failure of 40, 60, and 90 μm NiTi wires. The results of numerical modeling in the form of stress-strain curves are qualitatively and quantitatively similar to the experimental

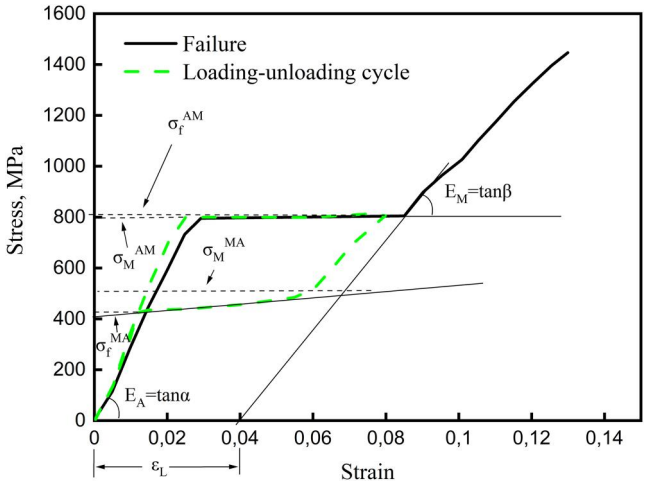

Figure 9. Stress-strain diagram for determining parameters of NiTi wire superelastic tensile behavior.

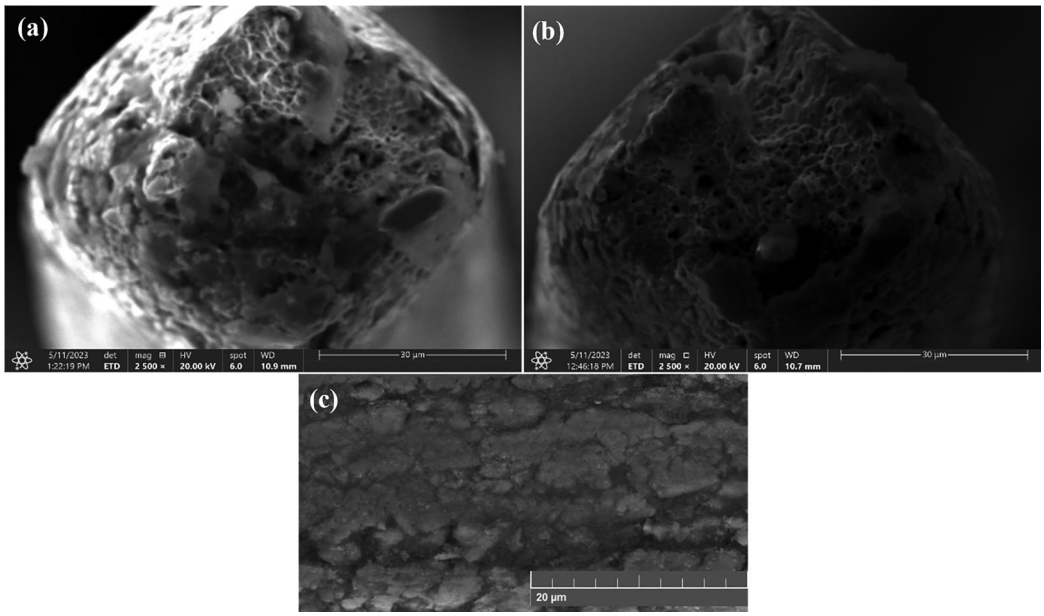

Figure 8. (a,b) 60 μm NiTi Wire fracture surfaces, (c) general view of the 60 μm NiTi wire side.

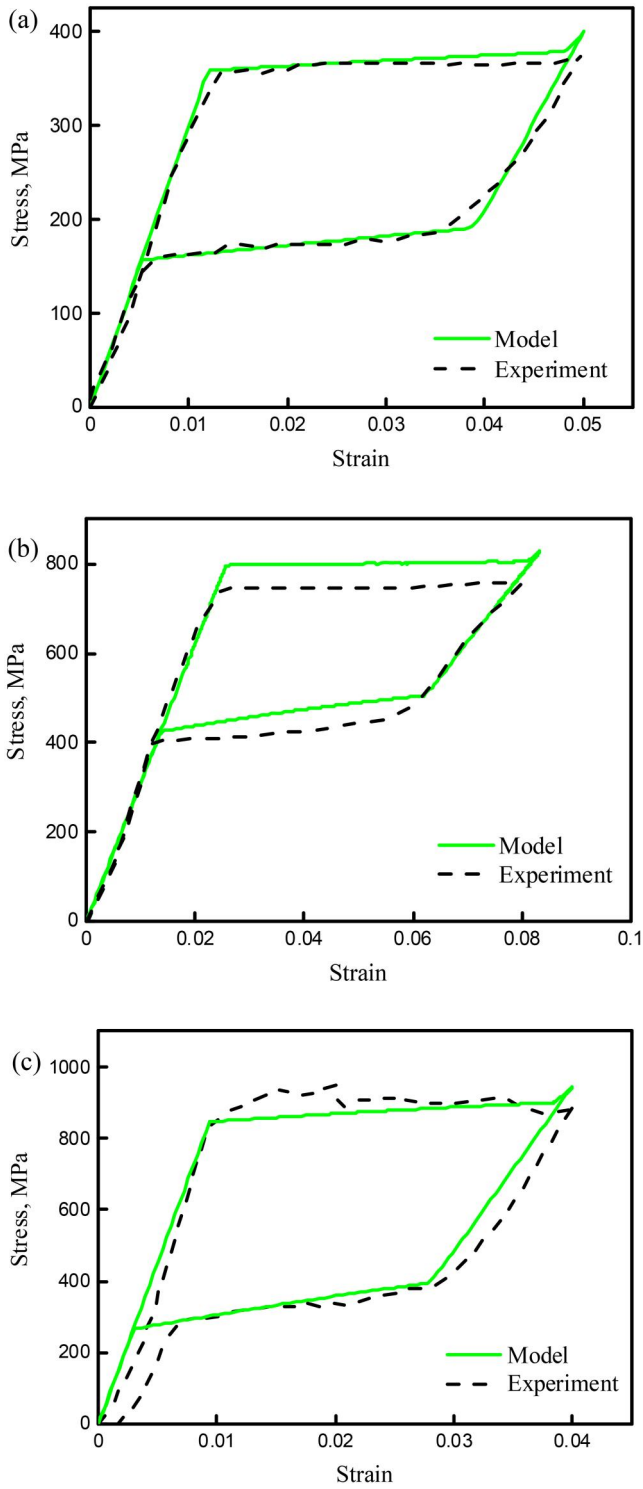

Figure 10. Comparison of experimental and calculated stress-strain curves of (a) 40 μm, (b) 60 μm, and (c) 90 μm NiTi wires loading-unloading cycle.

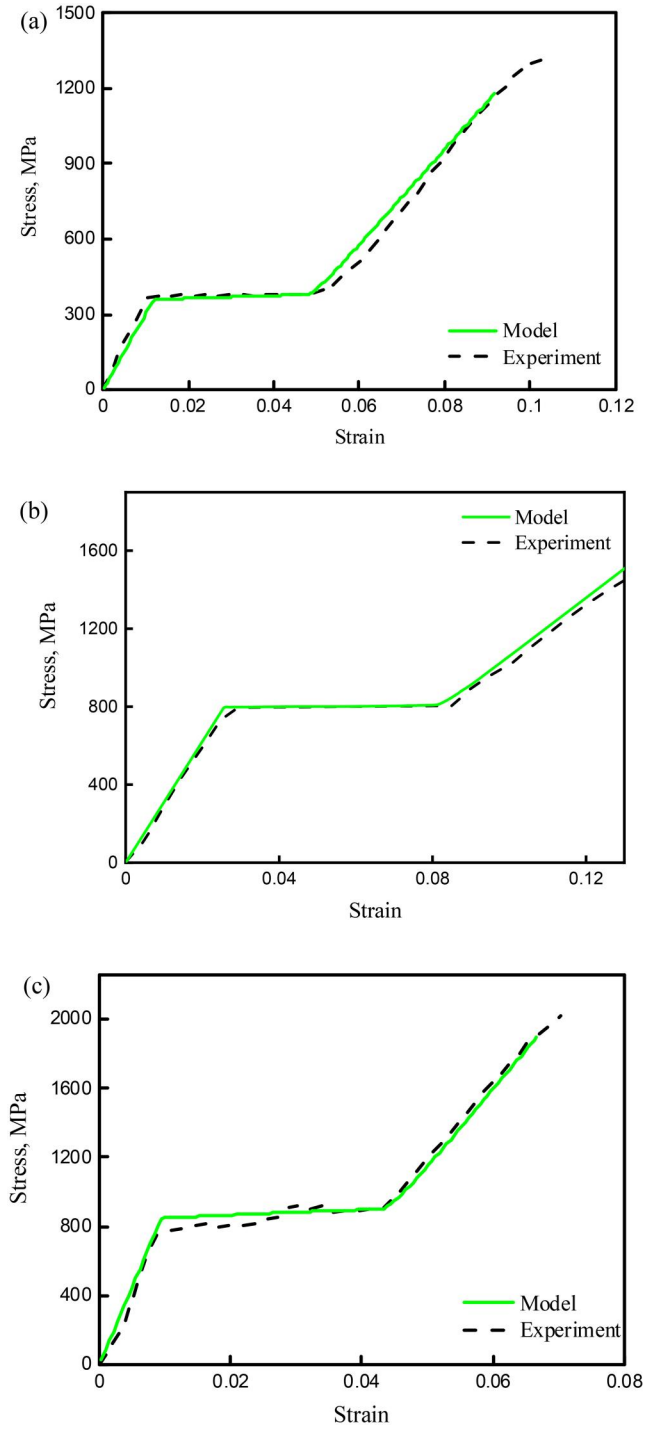

Figure 11. Comparison of experimental and calculated tensile stress-strain curves of (a) 40 μm, (b) 60 μm, and (c) 90 μm NiTi wires to failure.

data. This will make it possible to simulate the deformation behavior of superelastic NiTi wires and structures made from them.

4. Conclusions

Wire thinning and formation of a neck at rupture were discovered, which occurred due to the plastic shear of the viscous TiNi matrix. The fracture surface appears as a pitted relief, having a typical appearance with particles at the bottom of the dimples.

Elemental analysis showed a uniform distribution of titanium, nickel, and chlorine in the matrix, and an increased oxygen content in the surface layers, indicating a surface oxide layer formation. Based on the fracture surface observations and elements distribution, the wire outer shell, enriched in nonmetallic phases, fractured in a brittle manner, and the wire center, consisting of the viscous TiNi phase, fractured by the ductile mechanism.

All uniaxial tension stress-strain curves to rupture have three linear sections of elastic deformation, viscous flow, and linear hardening. The deformation behavior of all samples loaded cyclically is superelastic. The hysteresis width increases with the wire thickness. The obtained experimental stress-strain curves are typical for superelastic NiTi.

A finite element model was developed and tested to describe the superelasticity of the NiTi alloy. It is demonstrated that the Auricchio model is applicable for NiTi wires with diameters of 40, 60, and 90 μm, and the martensitic stress and tensile strength increase with the wire thickness.

Disclosure statement

No potential conflict of interest was reported by the author(s).

Funding

This research was supported by the Russian Science Foundation, No. 19-72-10105, https://rscf.ru/project/19-72-10105/.

ORCID

Ekaterina S. Marchenko http://orcid.org/0000-0003-4615-5270
Alexander A. Kozulin http://orcid.org/0000-0001-6711-3577
Anna V. Vetrova http://orcid.org/0000-0002-7605-6735
Marina A. Kovaleva http://orcid.org/0000-0001-6081-1751
Alex A. Volinsky http://orcid.org/0000-0002-8520-6248
Kirill M. Dubovikov http://orcid.org/0000-0003-0823-7208

References

[1] E.K. Kumar, S.S. Patel, S.K. Panda, B.K. Patle, E. Makki, and J. Giri, A comprehensive exploration of shape memory alloys: fundamentals, structural reinforcements, nano-analysis, machine learning perspective, and emerging applications, Mech. Adv. Mater. Struct., pp. 1–34, 2024. DOI: 10.1080/15376494.2024.2307471.

[2] T. Duerig, K. Melton, D. Stöckel, and C. Wayman, Wide hysteresis shape memory alloys. In: Engineering Aspects of Shape Memory Alloys, Butterworth-Heinemann, Oxford, pp. 130–136, 1990.

[3] S. Fähler, U.K. Rößler, O. Kastner, J. Eckert, G. Eggeler, H. Emmerich, P. Entel, S. Müller, E. Quandt, and K. Albe, Caloric effects in ferroic materials: new concepts for cooling, Adv. Eng. Mater., vol. 14, no. 1–2, pp. 10–19, 2012. DOI: 10.1002/adem.201100178.

[4] X. Moya, S. Kar-Narayan, and N. Mathur, Caloric materials near ferroic phase transitions, Nat. Mater., vol. 13, no. 5, pp. 439–450, 2014. DOI: 10.1038/nmat3951.

[5] J. Tušek, K. Engelbrecht, D. Eriksen, S. Dall'Olio, J. Tušek, and N. Pryds, A regenerative elastocaloric heat pump, Nat. Energy, vol. 1, no. 10, pp. 1–6, 2016. DOI: 10.1038/nenergy.2016.134.

[6] R. Snodgrass and D. Erickson, A multistage elastocaloric refrigerator and heat pump with 28 K temperature span, Sci. Rep., vol. 9, no. 1, pp. 18532, 2019. DOI: 10.1038/s41598-019-54411-8.

[7] J. Slaughter, A. Czernuszewicz, L. Griffith, and V. Pecharsky, Compact and efficient elastocaloric heat pumps—is there a path forward, J. Appl. Phys., vol. 127, no. 19, pp. 194501, 2020. DOI: 10.1063/5.0003275.

[8] T. Duerig, A. Pelton, and D. Stoeckel, An overview of nitinol medical applications, Mat. Sci. Eng. A., vol. 273–275, pp. 149–160, 1999. DOI: 10.1016/S0921-5093(99)00294-4.

[9] C. Cheng, Handbook of Vascular Motion, Elsevier—Academic Press, Cambridge, MA, 2019.

[10] E. Marchenko, Yu Yasenchuk, A. Vetrova, S. Gunter, G. Baygonakova, and A. Garin, Softening effect during cyclic stretching of titanium nickelide knitwear, Mech. Compos. Mater. Struct., vol. 27, no. 4, pp. 459–481, 2021. DOI: 10.33113/mkmk.ras.2021.27.04.459_481.02.

[11] E. Marchenko, Y. Yasenchuk, S.V. Gunther, A.A. Kozulin, A.V. Vetrova, A. Polonyankin, O.A. Fatyushina, and A.N. Vusik, Clinical use of titanium nickelide metal knitwear based on quantitative assessment of rheological similarity to soft biological tissues, Issues Reconstr. Plast. Surg., vol. 25, no. 2, pp. 68–81, 2022. DOI: 10.52581/1814-1471/81/07.

[12] E. Topolnitskiy, T. Chekalkin, E. Marchenko, and Yu Yasenchuk, Repair of huge thoracic defect combined with hernia after multimodality treatment of breast cancer, Respir. Med. Case Rep., vol. 34, pp. 101558, 2021. DOI: 10.1016/j.rmcr.2021.101558.

[13] E. Topolnitskiy, R. Mikhed, E. Marchenko, T. Chekalkin, and S. Gyunter, Replacement of an extensive chest wall defect in combination with the elimination of postoperative ventral hernia after combined treatment of breast cancer complicated by osteomyelitis of the sternum and ribs, Vestnik. Khirurgii. Imeni. Iigrekova, vol. 180, no. 2, pp. 78–82, 2021. DOI: 10.24884/0042-4625-2021-180-2-78-82.

[14] A. Chernyshova, L. Kolomiets, T. Chekalkin, V. Chernov, I. Sinilkin, V. Gunther, E. Marchenko, G. Baigonakova, and J.H. Kang, Fertility-sparing surgery using knitted TiNi mesh implants and sentinel lymph nodes: a 10-year experience, J. Invest. Surg., vol. 34, no. 10, pp. 1110–1118, 2021. DOI: 10.1080/08941939.2020.1745965.

[15] P. Sedlák, M. Frost, B. Benešová, T. Ben Zineb, and P. Šittner, Thermomechanical model for NiTi-based shape memory alloys including R-phase and material anisotropy under multi-axial loadings, Int. J. Plast., vol. 39, pp. 132–151, 2012. DOI: 10.1016/j.ijplas.2012.06.008.

[16] P. Sedmák, J. Pilch, L. Heller, J. Kopeček, J. Wright, P. Sedlák, M. Frost, and P. Šittner, Grain-resolved analysis of localized deformation in nickel-titanium wire under tensile load, Science, vol. 353, no. 6299, pp. 559–562, 2016. DOI: 10.1126/science.aad6700.

[17] M. Frost, B. Benešová, H. Seiner, M. Kružík, P. Šittner, and P. Sedlák, Thermomechanical model for NiTi-based shape memory alloys covering macroscopic localization of martensitic transformation, Int. J. Solids Struct., vol. 221, pp. 117–129, 2021. DOI: 10.1016/j.ijsolstr.2020.08.012.

[18] H. Tobushi, T. Nakahara, Y. Shimeno, and T. Hashimoto, Low-cycle fatigue of TiNi shape memory alloy and formulation of fatigue life, J. Eng. Mater. Technol., vol. 122, no. 2, pp. 186–191, 2000. DOI: 10.1115/1.482785.

[19] A. Runciman, D. Xu, A.R. Pelton, and R.O. Ritchie, An equivalent strain/Coffin–Manson approach to multiaxial fatigue and life prediction in superelastic nitinol medical devices, Biomaterials, vol. 32, no. 22, pp. 4987–4993, 2011. DOI: 10.1016/j.biomaterials.2011.03.057.

[20] K.R. Rajagopal and A.R. Srinivasa, On the bending of shape memory wires, Mech. Adv. Mater. Struct., vol. 12, no. 5, pp. 319–330, 2005. DOI: 10.1080/15376490590953581.

[21] M. Sreekumar, T. Nagarajan, and M. Singaperumal, Kinetostatic analysis of a spatial compliant mechanism actuated by three shape memory alloy wires in differential form, Mech. Adv. Mater. Struct., vol. 17, no. 3, pp. 225–236, 2010. DOI: 10.1080/15376490903556600.

[22] T. Videnic, M. Brojan, J. Kunavar, and F. Kosel, A simple one-dimensional model of constrained recovery in shape memory alloys, Mech. Adv. Mater. Struct., vol. 21, no. 5, pp. 376–383, 2014. DOI: 10.1080/15376494.2012.697599.

[23] F. Auricchio and A. Reali, A phenomenological one-dimensional model describing stress-induced solid phase transformation with permanent inelasticity, Mech. Adv. Mater. Struct., vol. 14, no. 1, pp. 43–55, 2007. DOI: 10.1080/15376490600864570.

[24] F. Auricchio and R.L. Taylor, Shape-memory alloys: modelling and numerical simulations of the finite-strain superelastic

behavior, Comput. Methods Appl. Mech. Eng., vol. 143, no. 1–2, pp. 175–194, 1997. DOI: 10.1016/S0045-7825(96)01147-4.

[25] L. Wang, J. Wang, Y. Xu, J. Zhu, and W. Zhang, Free vibration of pseudoelastic NiTi wire: finite element modeling and numerical design, Mech. Adv. Mater. Struct., vol. 31, no. 4, pp. 769–782, 2024. DOI: 10.1080/15376494.2022.2121990.

[26] R. Rizzoni, A. Chiozzi, M. Merlin, and A. Tralli, Comparative assessment of two constitutive models for superelastic shape-memory wires against experimental measurements, Mech. Adv. Mater. Struct., vol. 22, no. 9, pp. 731–747, 2015. DOI: 10.1080/15376494.2013.851752.

[27] A.J. Drelich, P.K. Bowen, L. LaLonde, J. Goldman, and J.W. Drelich, Importance of oxide film in endovascular biodegradable zinc stents, Surf. Innov., vol. 4, no. 3, pp. 133–140, 2016. DOI: 10.1680/jsuin.16.00014.

[28] H. Yang, C. Wang, C. Liu, H. Chen, Y. Wu, J. Han, Z. Jia, W. Lin, D. Zhang, W. Li, W. Yuan, H. Guo, H. Li, G. Yang, D. Kong, D. Zhu, K. Takashima, L. Ruan, J. Nie, X. Li, and Y. Zheng, Evolution of the degradation mechanism of pure zinc stent in the one-year study of rabbit abdominal aorta model, Biomaterials, vol. 145, pp. 92–105, 2017. DOI: 10.1016/j.biomaterials.2017.08.022.

[29] Y. Hou, X. Mi, H. Xie, W. Zhang, G. Huang, L. Peng, X. Feng, and Z. Yang, Size effect on mechanical properties and deformation behavior of pure copper wires considering free surface grains, Materials, vol. 13, no. 20, pp. 4563, 2020. DOI: 10.3390/ma13204563.

[30] G.A. Baigonakova, E.S. Marchenko, M.A. Kovaleva, E.A. Chudinova, A.A. Volinsky, and Y. Zhang, Thickness effects on the martensite transformations and mechanical properties of nanocrystalline NiTi wires, Nanomaterials, vol. 12, no. 24, pp. 4442, 2022. DOI: 10.3390/nano12244442.

[31] U. Ahmed, T. Hussain, and S. Abid, Role of knitted techniques in recent developments of biomedical applications: a review, JEFF, vol. 18, pp. 1–18, 2023. DOI: 10.1177/15589250231180293.

[32] S. Gunter, E. Marchenko, Y. Yasenchuk, G. Baigonakova, and A. Volinsky, Portable universal tensile testing machine for studying mechanical properties of superelastic biomaterials, Eng. Res. Express, vol. 3, no. 4, pp. 045055, 2021. DOI: 10.1088/2631-8695/ac41b4.

[33] F. Auricchio, A robust integration-algorithm for a finite-strain shape-memory-alloy superelastic model, Int. J. Plast., vol. 17, no. 7, pp. 971–990, 2001. DOI: 10.1016/S0749-6419(00)00050-4.

[34] G. Baigonakova, E. Marchenko, M. Kovaleva, and A. Vorozhtsov, Influence of wire geometry on the mechanical behavior of the TiNi design, Metals, vol. 12, no. 7, pp. 1131, 2022. DOI: 10.3390/met12071131.

[35] E. Marchenko, G. Baigonakova, S. Gunther, and O. Mamazakirov, Features of deformation of thin superelastic TiNi wire, Proceedings of 2022 ASM International – International Conference on Shape Memory and Superelastic Technologies, pp. 85–86, 2022. DOI: 10.31399/asm.cp.smst2022p0085.

[36] V.N. Khodorenko, M.I. Kaftaranova, and S.G. Anikeev, Functional properties of alloys based on titanium nickelide of different compositions, News High. Educ. Inst. Phys., vol. 57, no. 6/2, pp. 17–22, 2014.